

Calculation Method for External Thermal Load Heat Transfer in Civil Aircraft Fuel Systems

Zhengyifan Yang¹, Shuai Liu¹

¹ School of Safety Science and Engineering, Civil Aviation University of China, Tianjin 300300

Abstract: An approximate solution for the complex heat transfer of external fluid heat loads in civil aircraft fuel systems is provided in this article, with the wing fuel tank serving as an example. The skin is treated as a large flat plate, and the aim is to investigate the one-dimensional unsteady complex heat transfer law along the thickness direction of the flat plate. The research process introduces the penetration depth, penetration time, and dimensionless parameters of heat transfer, and the concept of the temperature distribution function is combined with the calculation methods of heat balance integral and approximate time integral to solve the inner surface temperature of the skin. The analytical and numerical solutions obtained by previous scholars are verified. It is demonstrated that the approximate solution method can be competent for calculating the heating process, with the absolute error controlled within 0.05. However, a more significant error is observed in the cooling process, with the absolute error controlled within 0.07, except for large radiation Biot numbers. The solution method can be applied to calculate the external heat load heat transfer of fuel tanks made of different materials, which is especially valuable for the study of airworthiness certification of composite fuel tanks.

Key Words: Fuel system; External heat load; Unsteady state heat transfer; Combined heat transfer; Airworthiness validation

1 Introduction

The heat load in civil aircraft fuel systems can be categorized into two main components: internal and external. Internally generated heat within the airframe originates primarily from electronic equipment, environmental control systems, sliding oil systems, hydraulic systems, and engine accessories. This heat is transferred to the fuel through direct or indirect means, but for the scope of this discussion, it is not under consideration. Conversely, external heat sources predominantly stem from solar radiation and aerodynamic heat transfer during flight. These external sources transmit heat to the fuel primarily through the aircraft's skin and the thermal insulation material of the fuel tank. In the case of wing fuel tanks, the fuel tank's boundary coincides with the airplane wing's skin. External factors such as solar radiation and aerodynamic heating influence the fuel temperature by affecting the skin.

In the context of the actual wing, it can be simplified as a flat plate due to the continuous variation of aircraft operating conditions. This heat transfer process is inherently non-steady-state owing to the dynamic nature of these conditions. As the civil aircraft industry gradually transitions from traditional metal materials to carbon fiber-reinforced composite materials for wing construction, the thermal resistance within the wing material increases. Consequently, the Biot number, which signifies the ratio of internal thermal resistance to external heat transfer, also increases. For a flat plate, when the Biot number surpasses 0.1, temperature errors exceeding 5% may arise, rendering analysis unsuitable for the centralized parameter method. The temperature variation across

the wing occurs solely along the thickness direction so that it can be treated as a one-dimensional, unsteady heat transfer problem.

In exploring one-dimensional unsteady heat transfer, Biot^[1] pioneered a variational method for analyzing transient heat flow within complex structures. This method significantly streamlines calculations and introduces fundamental concepts such as penetration depth and time. Biot's work laid the foundation for analyzing heat flow in supersonic wing structures. Building upon Biot's groundwork, Goodman^[2-4] introduced the "heat balance integral method," which leverages penetration depth and penetration time concepts. This method, also known as the "thermal equilibrium integral method", effectively converts second-order partial differential equations into ordinary differential equations, facilitating the derivation of approximate solutions. Moreover, it proves applicable to phase transition heat conduction problems. Subsequently, recognizing the nonlinear nature of boundary conditions in aircraft and missile structures, the thermal equilibrium integral method underwent further refinement to address nonconstant heat conduction problems. This enhanced method has garnered widespread adoption and refinement by numerous scholars in subsequent research endeavors. Its utilization addresses practical engineering challenges and enhances solution accuracy, marking a significant contribution to the field.

Drawing upon the example of wing surfaces, where the combined effects of convection and radiation are predominant, various analytical methods have been proposed to address this complex interaction. Liao et al.^[5] introduced an analytical approach grounded in inhomogeneous analysis to tackle the nonlinear model of joint cooling resulting from convection and radiation on spherical objects. This method offers a novel solution for resolving nonconstant nonlinear heat conduction challenges. Tan et al.^[6] developed an advanced set-total parameter model for transient heat conduction in walls experiencing combined convective and radiative cooling. A comparison with numerical solutions highlighted the superior predictive capabilities of the higher-order set-total model in estimating mean temperature compared to classical models. Crosbie et al.^[7] provided an approximate solution for transient heat transfer in flat plates under combined convective and radiative heating and cooling conditions. Davies et al.^[8], in their exploration of the joint convection and radiation action at boundaries, they utilized a flat plate as a particle shape approximation to study the flash dehydroxylation process of powdered kaolinite. They derived a semi-analytical solution for the flat plate's temperature distribution, validating its accuracy. Haseli et al.^[9] presented a novel semi-analytical solution for transient heat transfer in flat plates, accounting for heat exchange mechanisms with surroundings through convection, radiation, or simultaneous convection-radiation processes. Their expression demonstrated high accuracy in predicting surface temperatures across all scenarios. Given the limited applicability of exact analytical solutions to specific cases, significant research endeavors have been directed toward exploring approximate and numerical solutions to address the intricacies of combined convective and radiative heat transfer phenomena.

In this article, the fuel tank of a civil airplane wing serves as the focal point. By introducing concepts such as penetration depth and penetration time, coupled with the integration of temperature distribution functions, heat balance integrals, approximate time integrals, and other methodologies, an approximate solution method is proposed for addressing the one-dimensional unsteady heat transfer of a flat plate. This method is tailored to consider the operational conditions of the wing, including the combined effects of convection and radiation (excluding solar radiation) from the surrounding fluid. It offers computational convenience while maintaining sufficient accuracy in providing approximate solutions. Furthermore, the method's versatility allows its application to wing skins fabricated from various materials under typical operational scenarios.

2 Explanation of the operating environment of wing fuel tanks

In civil aircraft operations, different phases entail varying working environments, necessitating discussions on initial and boundary conditions tailored to each phase. A standard flight mission comprises five phases: takeoff taxiing, climbing, cruising, descending, and landing taxiing. Flight parameters such as altitude and Mach number fluctuate over time and can be represented as functions segmented by the parameter τ . Therefore, flight altitude is denoted as H and flight Mach number as Ma , accounting for their dynamic nature throughout the flight mission.

$$T^* = T_\infty \cdot \left[1 + \left(\frac{k-1}{2} \right) \cdot Ma^2 \right] \quad (1)$$

Where T^* represents the temperature of the stagnation point within the flow field surrounding the aircraft skin. T_∞ denotes the temperature of the ambient atmosphere, while k signifies the constant-pressure heat capacity of air. Additionally, Ma refers to the Mach number, a crucial parameter characterizing the aircraft's speed relative to the speed of sound.

In conditions of high-altitude flight, where the ambient temperature T_∞ varies with altitude, the atmospheric temperature variation can be illustrated based on findings from pertinent literature^[10], as depicted in Fig. 1.

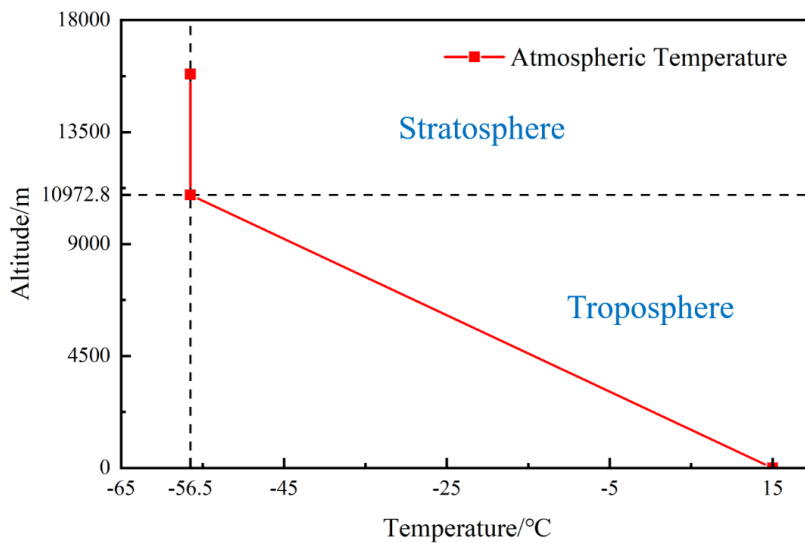


Figure 1 Patterns of change in atmospheric temperature

In standard conditions, the initial temperature at mean sea level in the troposphere is denoted as T_0 , and Δ represents the rate of temperature change with height (within the troposphere). The ambient temperature, T_∞ , can be expressed as follows

$$T_\infty = T_0 + \Delta \cdot H \quad (2)$$

Then, substituting Eq. 2 into Eq. 1 yields

$$T^* = (T_0 + \Delta \cdot H) \cdot \left[1 + \left(\frac{k-1}{2} \right) \cdot Ma^2 \right] \quad (3)$$

When computing the temperature distribution within civil aircraft structures, the choice of external convection heat transfer coefficient significantly impacts the accuracy of the results, consequently affecting crucial parameters such as fuel system temperature and other performance metrics. Various factors influence convection heat transfer according to the principles of heat transfer. These factors include the nature of fluid

flow (whether forced convection or natural convection), presence or absence of phase change in the fluid, flow state (laminar or turbulent), geometric characteristics of the heat transfer surface (shape, size, relative position to fluid flow direction, surface roughness, etc.), and fluid properties (thermal conductivity, dynamic viscosity, density, constant-pressure specific heat, etc.). For calculating the external convection heat transfer coefficient under flight conditions, consideration must be given to the significant Mach number and aerodynamic heating resulting from airflow compression and friction-induced obstruction. Therefore, accounting for gas compressibility and heat exchange effects is essential when determining the external convection heat transfer coefficient^[11–14]. Consequently, in forced convection conditions, the value of the fuselage's external convection heat transfer coefficient is solely dependent on flight altitude, velocity, and aircraft structure, independent of aircraft wall temperature.

In analyzing the convection heat transfer of an airplane wing, E. Pohlhausen introduced the boundary layer concept, illustrated in Fig. 2. At the starting point where $u=0$ and $y=0$, the fluid velocity experiences a sharp increase as y distance from the wall increases. Eventually, the velocity approaches the prevailing velocity after traversing a thin layer. This thin layer, known as the flow boundary layer, exhibits a thickness that varies depending on the degree of proximity to the mainstream velocity. Typically, the distance y at which 99% of the mainstream velocity is attained is the designated thickness of the flow boundary layer, denoted as δ .

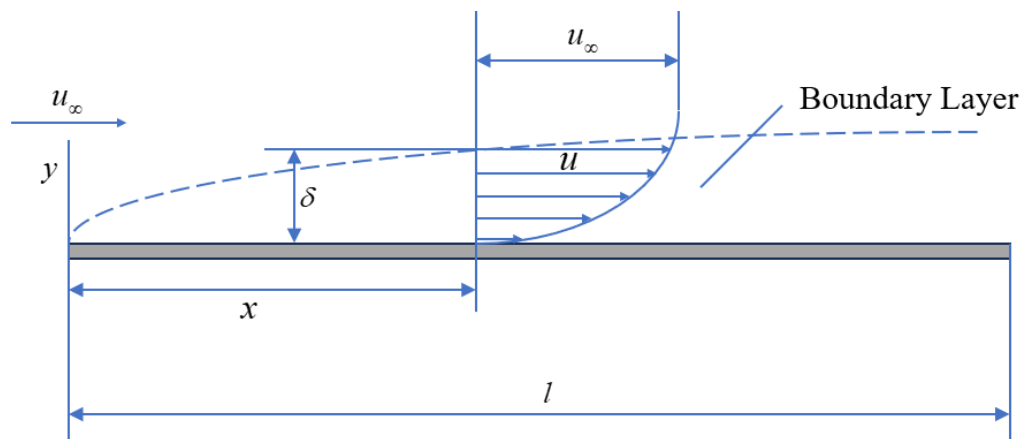


Figure 2 Boundary layer conditions for airflow along a flat plate

Hence, under the assumption of a constant surface temperature for the wing skin, solving the condition of $dp/dx=0$, as introduced in the boundary layer momentum equation, enables the derivation of analytical solutions for both the velocity and temperature fields within the cross-section during laminar flow. This analytical approach consequently facilitates the determination of the localized skin surface heat transfer coefficient.

$$h_x = 0.332 \frac{\lambda}{x} (\text{Re}_x)^{1/2} (\text{Pr})^{1/3} \quad (4)$$

where Re_x is the Reynolds number with x as the characteristic length. Eq. 4 can be reformulated as

$$\frac{h_x x}{\lambda} = 0.332 \text{Re}^{1/2} \text{Pr}^{1/3} \quad (5)$$

On the right-hand side of the equation above are two dimensionless numbers. The left-hand side must also be a dimensionless number, known as the Nusselt number and denoted as Nu_x , where the subscript x represents the characteristic length concerning the local geometry. To determine the convection heat transfer coefficient across the skin's entire surface, considering the discussed cases, the temperature differences used in calculating

the local heat transfer coefficients at different x are (T^*-T_0) , assuming fluid heating of the skin. Hence, integrating Eq. 4 from 0 to l straightforwardly yields.

$$Nu_l = 0.664 Re_l^{1/2} Pr^{1/3}$$

$$h_l = \frac{Nu_l \lambda}{l} = \frac{0.664 Re_l^{1/2} Pr^{1/3}}{l} \quad (6)$$

In Eqs. 4, 5, and 6 provided, Nu_l and Re_l signify that the characteristic length in both dimensionless numbers is the entire length of the skin, denoted as l . When applying these equations for specific calculations, it's crucial to consider that the physical properties of fluids are temperature-dependent. For convection heat transfer of the boundary layer type, it's stipulated that the average temperature of the fluids within the boundary layer, denoted as $T_m=(T^*+T_0)/2$, serves as the representative temperature. As indicated in reference^[15], it's observed that within the range of $Re \leq 2 \times 10^5$, the results obtained align well with experimental findings conducted on air.

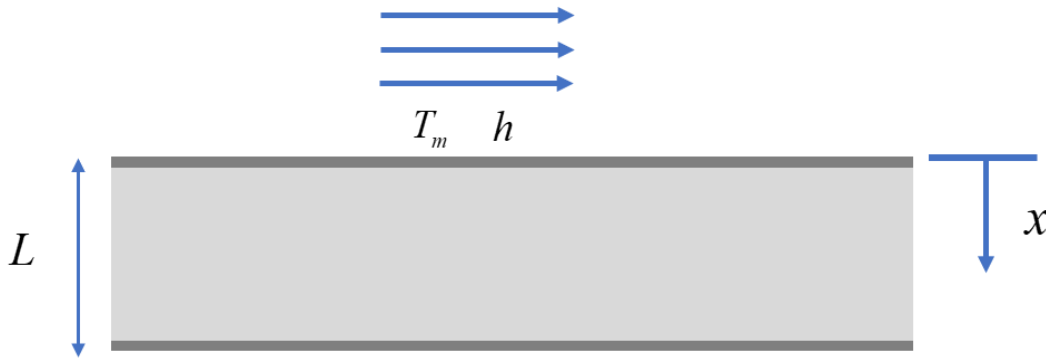


Figure 3 Simplified schematic of heat transfer in an aircraft wing

Upon analyzing the operational context of an aircraft wing, the wing skin can be conceptualized as an elongated flat plate with a thickness represented by L , as depicted in Fig. 3. Under the assumption of constant thermal physical properties and the absence of internal heat sources, the plate's outer side at $x=0$ facilitates heat transfer through convection with the external air. Conversely, at $x=L$, it represents the lower surface in contact with the internal fuel system. For this analysis, the heat transfer from the fuel tank's interior to the wing skin is disregarded, treating it as adiabatic. The schematic representation of the working environment is depicted in the accompanying figure. The initial and boundary conditions of this problem can be articulated as follows.

$$T(x, 0) = T_0 \quad 0 \leq x \leq L, \tau = 0 \quad (7)$$

$$-\lambda \frac{\partial T(0, \tau)}{\partial x} = q \quad x = 0, \tau \geq 0 \quad (8)$$

$$\frac{\partial T(L, \tau)}{\partial x} = 0 \quad x = L, \tau \geq 0 \quad (9)$$

where q represents the heat flow between the surface and its surroundings, encompassing various mechanisms such as thermal conductivity, convection, and radiation.

In the context of one-dimensional unsteady state heat transfer problems concerning flat plates, the heat transfer differential equation can be expressed as

$$\rho c_p \frac{\partial T}{\partial \tau} = \frac{\partial}{\partial x} \left(\lambda \frac{\partial T}{\partial x} \right)$$

$$\alpha \frac{\partial^2 T}{\partial x^2} = \frac{\partial T}{\partial \tau} \quad 0 \leq x \leq L, \tau \geq 0 \quad (10)$$

where $T=T(x,\tau)$ represents the temperature at position x at time τ , where α denotes the thermal diffusion coefficient of the flat plate, this coefficient is defined as $\alpha=\lambda/(\rho c_p)$, where λ signifies the heat transfer coefficient, ρ represents density, and c_p denotes specific heat.

Following Biot's concept of thermal penetration depth, the heat wave propagates through the thickness of the flat plate over time, inducing a temperature gradient within the plate. This thermal penetration depth is expressed as δ_τ . Consequently, the boundary condition can be formulated as

$$\frac{\partial T(\delta_\tau, \tau)}{\partial x} = 0 \quad (11)$$

Utilizing the notion of heat penetration depth alongside the heat balance integration method applied to Eq. 10 results in

$$\int \frac{\partial T}{\partial \tau} dx = \frac{\alpha}{\lambda} q \quad 0 \leq x \leq \delta_\tau \quad (12)$$

Assuming that the temperature distribution within the flat plate can be approximated by a quadratic polynomial $T=ax^2+bx+c$, where the coefficients are functions of τ , one can deduce, based on the boundary conditions of Eqs. 8 and 11, that T follows

$$T = T_0 + \frac{q\delta_\tau}{2\lambda} \left(1 - \frac{x}{\delta_\tau}\right)^2 \quad (13)$$

Substituting Eq. 13 into Eq. 12 yields

$$\int \frac{\partial T}{\partial \tau} dx = \frac{d}{d\tau} \left(\frac{q\delta_\tau^2}{6\lambda} \right) \\ \frac{d}{d\tau} (q\delta_\tau^2) = 6\alpha q \quad (14)$$

Eq. 13 depicts the temperature distribution where the heat wave does not penetrate the flat plate. However, a quadratic polynomial can still represent the temperature distribution inside if the heat wave penetrates the plate.

$$T = T_a - \frac{q}{\lambda} x + \frac{q}{2\lambda L} x^2 \quad (15)$$

Applying the same substitution of Eq. 15 to Eq. 12 results in

$$\int \frac{\partial T}{\partial \tau} dx = \frac{d}{d\tau} \left(T_a L - \frac{qL^2}{3\lambda} \right) \\ \frac{d}{d\tau} \left(T_a L - \frac{qL^2}{3\lambda} \right) = \frac{\alpha}{\lambda} q_s \quad (16)$$

Eq. 14 and Eq. 16 will serve as essential components in the subsequent solution process for the heat transfer mechanism outlined in the later section.

3 Calculation of heat transfer for external thermal loads

This chapter will explain the three forms of calculations regarding convection heat transfer, radiation heat transfer, and combined convective and radiative heat transfer.

3.1 Convection Calculation on Wing Skin Surface

This section outlines the computation of surface convection in the wing skin, where the heat flow generated by surface convection can be formulated as

$$q = h(T_m - T_a) \quad (17)$$

In this equation, h represents the convection heat transfer coefficient, T_m represents the fluid temperature outside the skin, and T_a denotes the temperature outside the skin. Considering the aircraft's operational conditions, scenarios exist where $T_m > T_a$ and $T_m < T_a$. In cases where $T_m > T_a$, the heat flow is positive, indicating a convection heating process. Conversely, when $T_m < T_a$, the heat flow is negative, signifying a convective cooling process.

Substituting Eq. 17 into Eq. 13 yields

$$T_a = T_m + \frac{T_0 - T_m}{1 + \frac{B_i \delta}{2}} \quad (18)$$

where B_i denotes the Biot number, calculated as $B_i = (L/\lambda)/(1/h)$, and $\delta = \delta_r/L$ represents the dimensionless thermal penetration depth.

By introducing the excess temperature $\theta = T - T_m$, the initial condition for the excess temperature is represented as $\theta(0) = T_0 - T_m = \theta_0$. Eq. 13 is then compiled and normalized to derive the distribution of the excess temperature within the flat plate.

$$\Theta = \frac{\theta}{\theta_0} = 1 - \frac{B_i \delta}{2 + B_i \delta} \left(1 - \frac{\eta}{\delta}\right)^2 \quad 0 \leq \eta \leq \delta \quad (19)$$

In this context, the excess temperature θ to the initial excess temperature θ_0 ratio is represented by the dimensionless parameter Θ . Additionally, the dimensionless position is denoted by $\eta = x/L$.

Eq. 17 and Eq. 18 are substituted into Eq. 14, followed by an approximate time integral to represent the time corresponding to a specific penetration depth. Notably, in this context, the heat flow in Eq. 15 needs to be considered as the average of the initial moment ($Fo=0$) heat flow $q_0 (=h_0(T_m - T_0))$ and a particular moment in time of the heat flow $q^{[16]}$. Thus

$$Fo = \frac{\delta^2}{\left(3\delta + \frac{6}{B_i}\right) \ln\left(1 + \frac{B_i \delta}{2}\right) + \left(3 + \frac{3}{2} B_i \delta\right) \frac{h_0}{h}} \quad (20)$$

Here, the Fourier number $Fo = \tau/(L^2/\alpha)$ is introduced, where the numerator τ represents the time interval from the moment when the thermal perturbation initiates at the boundary of the flat plate to the moment of calculation. The denominator L^2/α can be understood as the time required for the thermal perturbation of finite size at the boundary to diffuse through the flat plate of a certain thickness to an area of L^2 . Consequently, the Fourier number serves as a dimensionless time, characterizing the depth of the unsteady state process. It encapsulates the depth at which the unsteady process unfolds. The process of heat wave penetration through the flat plate is delineated into two consecutive phases, with the first phase's end moment aligning with the second phase's beginning moment. At this juncture, the dimensionless penetration depth $\delta=1$ is derived by substituting Eq. 20.

$$Fo_p = \frac{1}{\left(3 + \frac{6}{B_i}\right) \ln\left(1 + \frac{B_i}{2}\right) + \left(3 + \frac{3}{2} B_i\right) \frac{h_0}{h}} = \frac{1}{\left(3 + \frac{6}{B_i}\right) \ln\left(1 + \frac{B_i}{2}\right)} \quad (21)$$

This moment can be designated as the heat penetration time, denoted as Fo_p . Here, h_0 represents the convection heat transfer coefficient of the aircraft at the moment just before it starts on the ground. According to Eq. 8, it can be assumed that $h_0 \approx 0$.

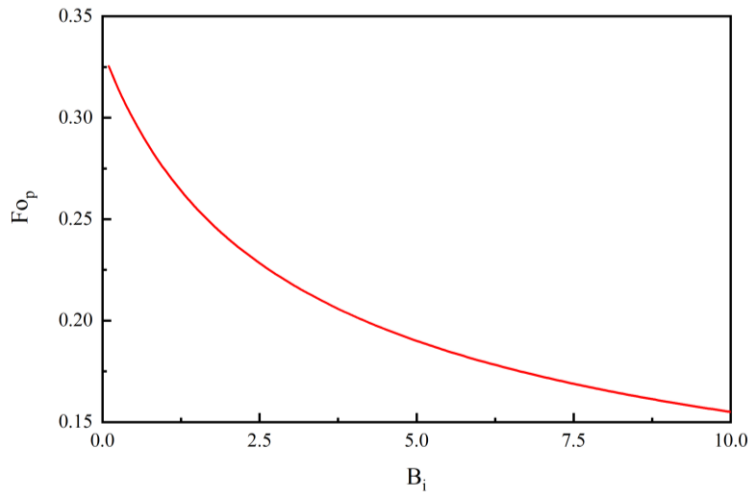


Figure 4 Variation of heat penetration time with Biot number under convection

Fig. 4 illustrates the heat penetration time Fo_p for various Biot number values, ranging from 0.1 to 10. The corresponding Fo_p values fall within the range of 0.155 to 0.3253. At the Fo_p moment, substituting $\delta=1$ and $\eta=0$ into Eq. 19 yields the excess temperature $\theta_a^p/\theta_0=2/(2+B_i)$ at the outer position of the flat plate. Combining this result with Eqs. 15, 16, and 17 enables the derivation of the excess temperature distribution within the flat plate after the heat wave penetration.

$$\Theta = \frac{2}{2+B_i} \cdot e^{-\frac{B_i}{3+B_i}(Fo-Fo_p)} \cdot \left(1+B_i\eta - \frac{B_i}{2}\eta^2\right) \quad (22)$$

3.2 Radiation Calculation on Wing Skin Surface

This section delineates the computation of surface radiation for the wing skin, where the heat flow induced by surface radiation can be formulated as

$$q = \varepsilon\sigma(T_m^4 - T_a^4) \quad (23)$$

where ε represents the emissivity of the aircraft skin, while σ denotes the Stefan-Boltzmann constant. Similar to convection calculations, adopting a convention where positive heat flow signifies radiative heating and negative heat flow signifies radiative cooling remains consistent.

Substituting Eq. 23 into Eq. 14 and employing approximate time integration, once more, it's essential to consider the heat flow in Eq. 14 as the average between the heat flow $q_0(=\varepsilon\sigma(T_m^4-T_0^4))$ at the initial moment ($Fo=0$) and the heat flow q at the moment of Fo . Thus

$$\delta^2 = 3Fo \left(1 + \frac{q_0}{q}\right) \quad (24)$$

$$Fo = \frac{\delta^2}{3} \left(\frac{1-t_a^4}{2-t_a^4-t_0^4}\right) \quad (25)$$

Eq. 25 defines $t=T/T_m$ as the dimensionless temperature. Combining Eq. 13 and Eq. 23 provides the temperature distribution before the heat wave penetrates the flat plate.

$$\Theta = 1 - \frac{B_i^r}{2} \frac{1-t_a^4}{1-t_0^4} \left(1 - \frac{\eta}{\delta}\right)^2 \quad 0 \leq \eta \leq \delta \quad (26)$$

Eq. 26 introduces the concept of the radiation Biot number^[9], denoted as $B_i^r(=T_m^3L\varepsilon\sigma/\lambda)$, which is also a dimensionless parameter. Similar to Eq. 19, which is applicable only during the initial stage of heat wave

penetration for $0 \leq \delta \leq 1$, it becomes necessary once more to compute F_{op} at the precise moment when the heat wave penetrates the flat plate entirely. This involves substituting $\delta=1$ into Eq. 25.

$$F_{op} = \frac{1}{3} \left(\frac{1-t_a^4}{2-t_a^4-t_0^4} \right) \quad (27)$$

If the process involves radiative heating of the skin from the outside, then $t_0 < t_a \leq 1$; conversely, if it entails radiative cooling of the skin to the outside, then $1 < t_a < t_0$.

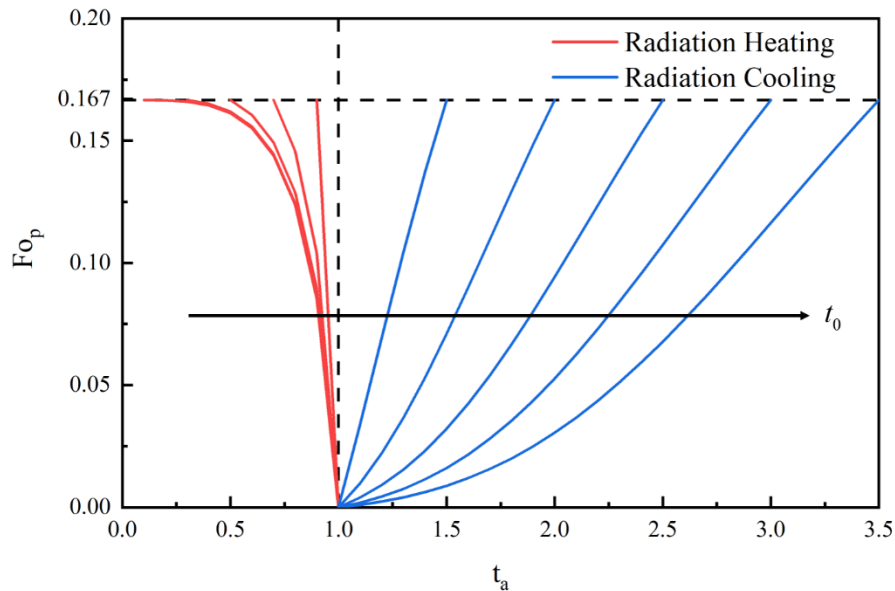


Figure 5 Variation of heat penetration time with inner surface temperature of the skin under radiation

Fig. 5 illustrates the heat penetration time F_{op} values in 10 cases based on the abovementioned scenarios, where t_0 takes values of 0.1, 0.3, 0.5, 0.7, 0.9, 1.5, 2.0, 2.5, 3.0, and 3.5, respectively. It can be observed that the values of F_{op} fall within the range of $[0, 0.167]$, albeit with varying trends for each graph. By combining Eqs. 15, 16, and 23, the temperature distribution after the penetration of the heat wave can be determined.

$$\Theta = \frac{t_a - 1}{t_0 - 1} + \frac{B_i^r}{2} \frac{1-t_a^4}{1-t_0^4} (2\eta - \eta^2) \quad (28)$$

3.3 Combined Convection and Radiation Computation on Wing Skin Surface

This section delineates the combined calculation of convection and radiation on the surface of the wing skin. The heat flow resulting from the combination of convection and radiation on its surface can be expressed as

$$q = h(T_m - T_a) + \varepsilon\sigma(T_m^4 - T_a^4) \quad (29)$$

Eq. 29 also distinguishes between positive and negative values, where a positive number denotes a combined-acting heating process, and a negative number indicates a combined-acting cooling process.

The Fourier number can also be calculated through approximate time integration. This involves considering the average heat flow at the initial moment ($Fo=0$), represented by $q_0(=h_0(T_m-T_0)+\varepsilon\sigma(T_m^4-T_0^4))$, with Eq. 29. Subsequently, this value is substituted into Eq. 14. According to Eq. 30, the process is expressed in a dimensionless form as

$$Fo = \frac{\delta^2}{3} \left(\frac{B_i^r (1-t_a^4) + B_i (1-t_a)}{B_i^r (2-t_a^4-t_0^4) + B_i (1-t_a) + B_{i_0} (1-t_0)} \right) = \frac{\delta^2}{3} \left(\frac{B_i^r (1-t_a^4) + B_i (1-t_a)}{B_i^r (2-t_a^4-t_0^4) + B_i (1-t_a)} \right) \quad (30)$$

Here, it is assumed that $h_0 \approx 0$, hence $B_{i_0} \approx 0$. Consequently, Eq. 13 and Eq. 29 are combined and organized to derive the temperature distribution during the heat wave penetration process.

$$\Theta = 1 - \frac{1}{2} \frac{B_i^r (1-t_a^4) + B_i (1-t_a)}{1-t_0} \left(1 - \frac{\eta}{\delta} \right) \delta \quad 0 \leq \eta \leq \delta \quad (31)$$

Substituting $\delta=1$ into Eq. 31, the heat penetration time Fo_p for the combined effect of convection and radiation can be obtained.

$$Fo_p = \frac{1}{3} \left(\frac{B_i^r (1-t_a^4) + B_i (1-t_a)}{B_i^r (2-t_a^4-t_0^4) + B_i (1-t_a)} \right) \quad (32)$$

The temperature distribution following the penetration of the heat wave can also be determined by referencing Eqs. 15, 16, and 29.

$$\Theta = \frac{t_a - 1}{t_0 - 1} + \frac{1}{2} \frac{B_i^r (1-t_a^4) + B_i (1-t_a)}{1-t_0} (2\eta - \eta^2) \quad (33)$$

4 Verification

This section is dedicated to verifying the accuracy of the expressions for excess temperature resulting from convection, radiation, and combined convection and radiation.

4.1 Verification of Convection

A simplified expression for convection is commonly provided in heat transfer textbooks for the analytical solution of flat plate problems.

$$\frac{\theta(\eta, \tau)}{\theta_0} = \frac{2 \sin \mu_1}{\mu_1 + \sin \mu_1 \cos \mu_1} e^{-\mu_1^2 Fo} \cos[\mu_1 (\eta - 1)] \quad (34)$$

Fig. 6 illustrates the curve of the flat plate μ_1 as a function of B_i . It demonstrates that the dimensionless excess temperature θ/θ_0 of the flat plate is associated with the Fourier number, the Biot number, and the dimensionless distance η , expressed as $\theta/\theta_0=f(Fo, B_i, \eta)$.

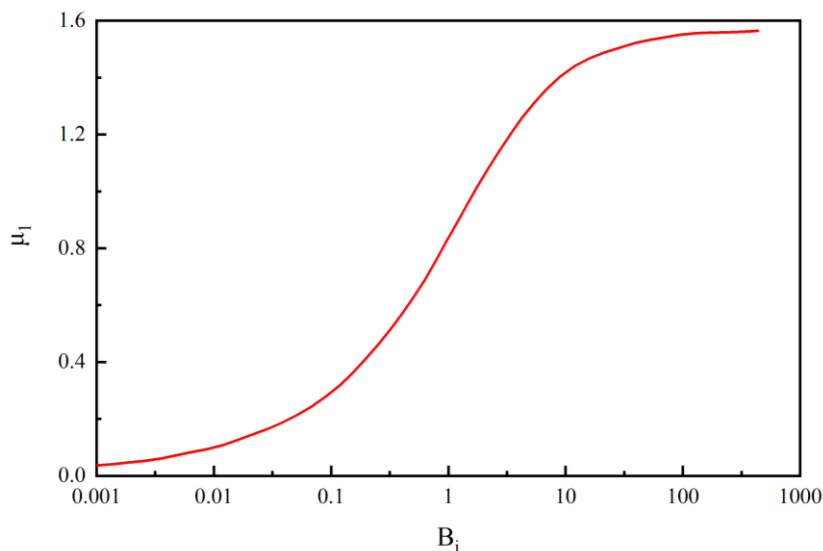


Figure 6 Variation of eigenvalues of flat analytic solutions with B_i

In engineering, the focus typically centers on the temperature of the inner side of the skin, represented by the dimensionless excess temperature θ_b/θ_0 at the position $\eta=1$. Consequently, it is feasible to align $\eta=1$ with the curves of the analytical solution (Eq. 34) and the approximate solution (Eqs. 19 and 22) at this position for various Fourier and Biot numbers. Referring to Fig. 6, it can be observed that when B_i is set to 0.1, 1, and 10, μ_1 equals 0.29766, 0.83549, and 1.5518, respectively.

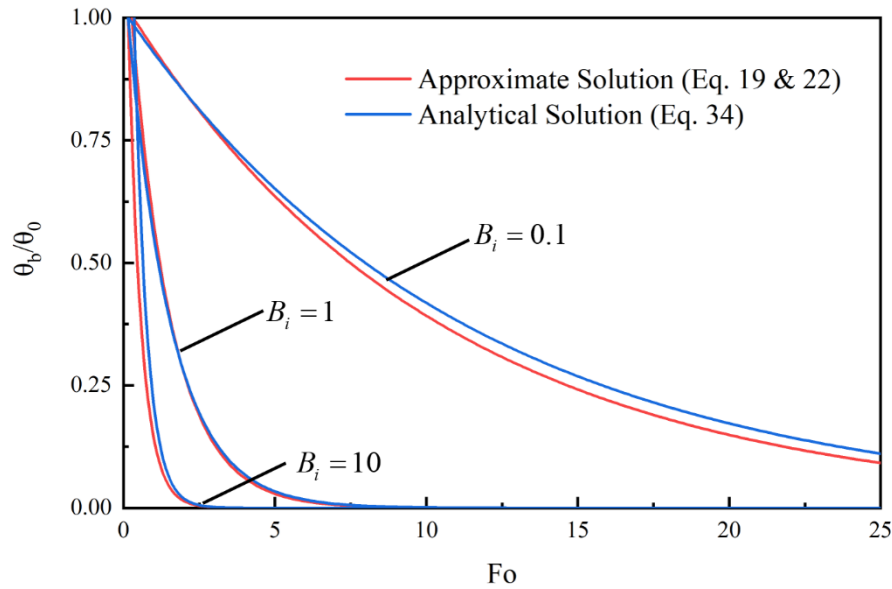


Figure 7 Comparison of approximate and analytical solutions for the inner skin temperature under convection for $B_i=0.1, 1$ and 10

Fig. 7 depicts the analytical and approximate solution curves for various Fourier and Biot numbers for the dimensionless excess temperature θ_b/θ_0 . The plots exhibit optimal alignment when the Biot number is set to 1. Furthermore, the absolute error can be kept within 0.03 in the other two cases.

4.2 Verification of Radiation

Verifying the radiation aspect relies on numerical solutions due to the absence of an analytical solution in a specific form. This involves discretizing the problem into finite difference forms based on Eq. 10 and Eq. 23.

Based on Eq. 10

$$\frac{T_i^{n+1} - T_i^n}{\Delta \tau} = \alpha \frac{T_{i+1}^n - 2T_i^n + T_{i-1}^n}{\Delta x^2} \quad (35)$$

Based on Eq. 23

$$\frac{q_i^{n+1} - q_i^n}{\Delta \tau} = \varepsilon \sigma (T_m^4 - T_i^n)^4 - \varepsilon \sigma (T_m^4 - T_i^{n+1})^4 \quad (36)$$

The numerical solution was tackled using MATLAB/Simulink. Similar to the validation process for convection action, the focus remains on the temperature of the inner surface of the skin, namely the dimensionless excess temperature θ_b/θ_0 at position $\eta=1$.

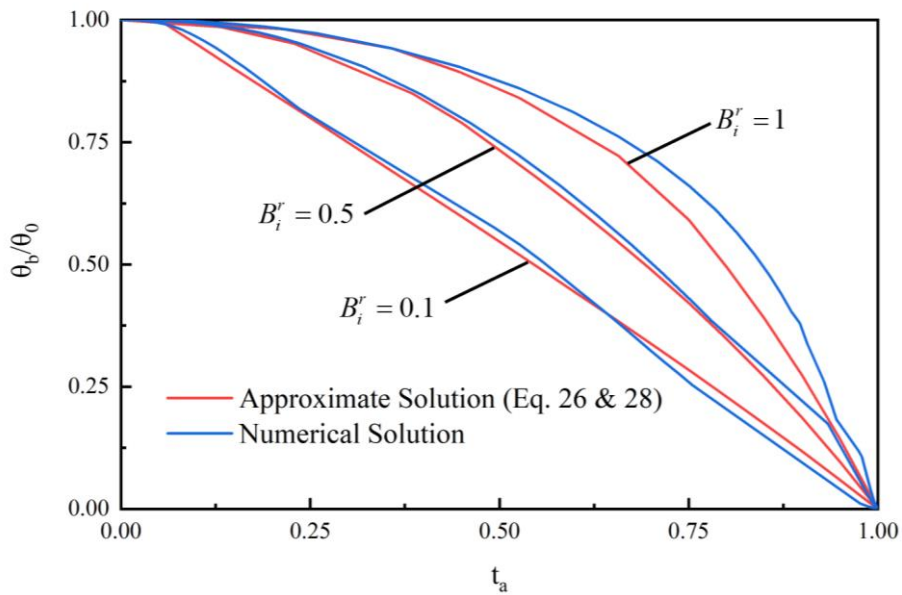


Figure 8 Comparison of approximate and numerical solutions of inner skin temperature for $B_i^r=0.1, 1$ and 10 under radiation heating

As depicted in Fig. 8, with η set to 1 and t_0 to 0, assuming a radiative heating process, the results from both the approximate solution and the numerical solution are presented for three scenarios: radiation Biot numbers of 0.1, 0.5 and 1. It's evident that the error of the approximate solution gradually increases with higher B_i^r values. Optimal fit and higher accuracy are achieved when B_i^r takes smaller values, ensuring the calculation results are more precise, with the absolute error controlled within 0.05. However, when B_i^r is 1, the maximum absolute error reaches 0.1.

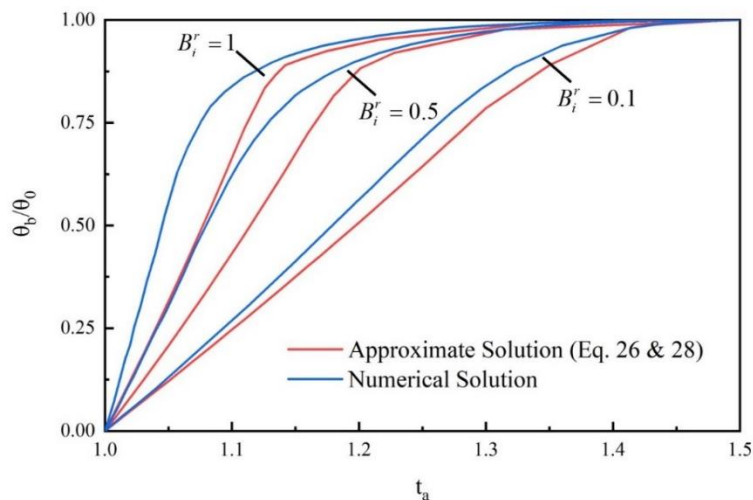


Figure 9 Comparison of approximate and numerical solutions of inner skin temperature for $B_i^r=0.1, 1$ and 10 under radiation cooling

Similarly, setting η to 1 and t_0 to 1.5, assuming a radiation cooling process, Fig. 9 illustrates the results obtained from both the approximate and the numerical solutions for three cases with radiation Biot numbers of 0.1, 0.5, and 1. Similar to the radiative heating process, the error of the approximate solution gradually increases

with higher B_i^r values. When B_i^r takes smaller values, the calculation results are more accurate, with the absolute error controlled within 0.07.

4.3 Verification of Combined Convection and Radiation

Similar to the approach for verifying radiation, no specific analytical solution is available for the combined convection and radiation scenario, necessitating validation through numerical methods. The focus remains on the inner surface temperature of the skin, with η set to 1 and various values of the Biot number and radiation Biot number considered, respectively.

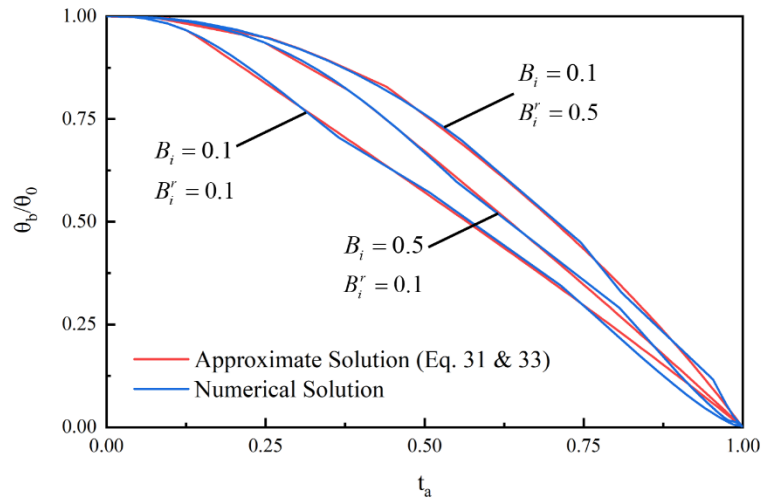


Figure 10 Comparison of approximate and numerical solutions for inner skin temperature under combined convective and radiative heating

Due to the significant error observed when the radiation Biot number is set to 1, this validation session excludes $B_i^r=1$. Illustrated in Fig. 10, with $\eta=1$ and $t_0=0$, assuming a combined convective and radiative heating process, the plots of the approximate and numerical solutions are depicted for Biot numbers of 0.1 and 0.5 and radiation Biot numbers of 0.1 and 0.5, yielding three combinations. The plots exhibit a good fit, with absolute errors not exceeding 0.03.

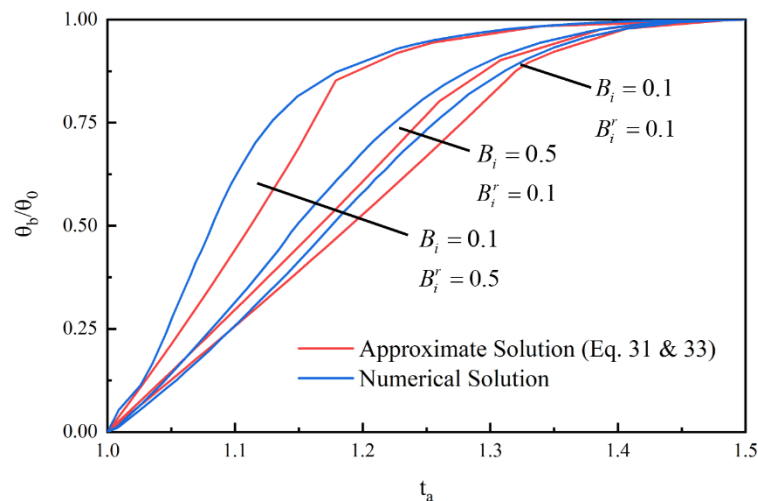


Figure 11 Comparison of approximate and numerical solutions for inner skin temperature under combined convective and radiative cooling

Illustrated in Fig. 11, with $\eta=1$ and $t_0=1.5$, assuming a combined convective and radiative cooling process, the plots of the approximate and numerical solutions are displayed for three combinations: Biot numbers of 0.1 and 0.5, and radiation Biot numbers of 0.1 and 0.5. The plot lines exhibit better fit in the cases with a radiation Biot number of 0.1, with the absolute error remaining within 0.07.

The verification confirms the reliability of the approximate solution for convection, with error rates escalating with higher radiation Biot numbers for both radiation and combined convective and radiative scenarios. Generally, solving skin heating processes yields higher accuracy than skin cooling processes, with absolute errors in inner skin excess temperature typically kept below 0.07.

5 Analysis of heat transfer influencing factors

The graphs presented in Chapter 4 serve as a validation tool to explore additional heat transfer influences and patterns. Through separate analyses, one can discuss the potential implications of changes in aircraft operating conditions, thereby enriching the understanding of heat transfer dynamics.

(1) Assuming no change in aircraft operating conditions

Assuming a constant operating condition for the airplane implies that the flight altitude and flight Mach number remain unchanged, thereby keeping the convective heat transfer coefficient between the wing and the external fluid constant. The variation in the Biot number indicates alterations in the skin material properties, particularly thermal conductivity. As for the radiation Biot number, maintaining constancy involves controlling factors such as the average temperature of the boundary layer, skin thickness, Stefan-Boltzmann constants, and material properties. Neglecting variations in the thermal conductivity of the skin material and changes in the emissivity of the skin material can be reflected through adjustments in the radiation Biot number.

Analyzing Fig. 7 reveals that with an increasing Biot number, the temperature on the inner side of the skin approaches ambient temperature at a lower Fourier number. This phenomenon occurs because a higher Biot number signifies a more rapid heat transfer rate from the skin's surface compared to its interior. Consequently, the heat flow penetrates the skin's thickness more swiftly, driven by the rapid surface temperature elevation due to increased surface heat transfer. This dynamic amplifies the internal temperature gradient, expediting the heat transfer rate. Conversely, a smaller Biot number signifies a relatively more significant internal heat transfer rate, resulting in slower heat flow penetration into the skin.

The radiation Biot number is known to be proportional to the emissivity of the skin material. Referring to Fig. 8 and Fig. 9, an increase in the radiation Biot number indicates that the heat transfer rate from the skin surface surpasses that from the interior. Consequently, there is a rapid rise in the temperature of the outer skin surface, while the change in temperature of the inner skin surface remains insignificant. As a result, regardless of whether it is a heating or cooling process for the skin, a large temperature gradient will emerge when the radiation Biot number is high.

Based on the analysis above, it's evident that an increase in either dimensionless parameter, whether the Biot number or the radiation Biot number, leads to a more significant temperature gradient. Referring to Figs. 10 and 11, it becomes clear that an increase in the radiation Biot number can induce a more significant temperature gradient compared to an increase in the Biot number, observed in both skin heating and cooling processes.

(2) Assuming a change in aircraft operating conditions

Assuming a shift in the airplane's operating conditions, such as alterations in flight altitude and Mach

number, Eq. 6 indicates that the convection heat transfer coefficient between the wing and the external fluid will vary due to changes in flight speed. Concerning the Biot number, the constancy of skin material properties ensures that alterations in the strength of the convection heat transfer effect are reflected through changes in the Biot number. Regarding Eqs. 2 and 3 and the concept of qualitative temperature, it's evident that the average temperature in the boundary layer is influenced by flight altitude and Mach number. Regarding the radiation Biot number, maintaining the skin's thickness, keeping Stefan-Boltzmann constant, and keeping skin material unchanged allows for the reflection of variations in boundary layer temperature. Changes in the radiation Biot number effectively mirror shifts in the boundary layer temperature, provided that the effects of temperature on the thermal conductivity and emissivity of the skin material are disregarded.

Based on the observations from Fig. 7, it becomes apparent that as the Biot number increases, so does the convection heat transfer coefficient. This escalation underscores the pronounced influence of convection, leading to a rapid rise in the temperature of the outer skin surface. Consequently, this escalation fosters the formation of a more substantial temperature gradient, even when the thermal conductivity of the skin remains constant.

As depicted in both Fig. 8 and Fig. 9, an increase in the radiation Biot number corresponds to a higher average temperature within the boundary layer. This elevation in temperature difference, as delineated by Eq. 23, amplifies the intensity of heat flow on the outer side of the skin, thereby accentuating the radiation effect. Consequently, the outer surface temperature of the skin converges more rapidly towards the surrounding temperature, ultimately engendering a more pronounced internal temperature gradient.

In both Figs. 10 and 11, the compounded effect of altering aircraft operating conditions is evident. Specifically, it illustrates that the average boundary layer temperature has a more pronounced impact on increasing the temperature gradient within the skin compared to the influence of the convection heat transfer coefficient.

In engineering practice, considerations extend beyond merely assessing the magnitude of the temperature gradient. For instance, in May 2008, the FAA introduced the Fuel Tank Flammability Analysis Method (FTFAM), also referred to as the Monte Carlo Analysis Method^[17], through its official website. This method, rooted in the Monte Carlo Random Number Technique, is instrumental in evaluating the fuel tank flammability standard stipulated in CCAR 25.981. It underscores the significance of the fuel tank temperature as a pivotal factor in assessing the fuel tank flammability standard and determining airworthiness certification.

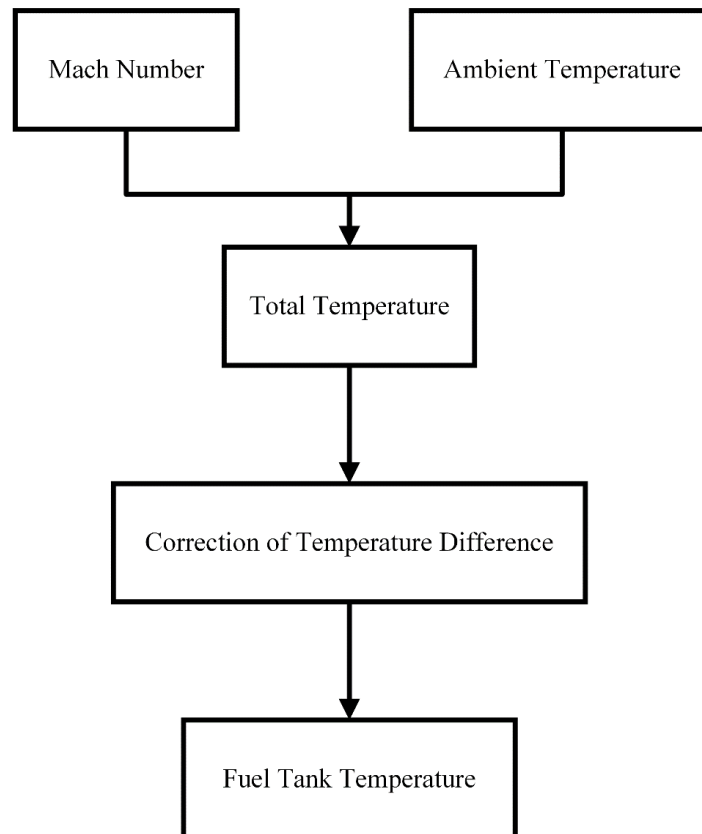


Figure 12 Part of the workflow of the fuel tank flammability assessment program

Fig. 12 depicts a segment of the workflow involved in the fuel tank flammability assessment program, emphasizing the significance of the inner skin surface temperature magnitude over a defined timeframe. In practical applications, it's common for aircraft operating conditions to undergo compounded changes. Regarding the duration required for heat flow to reach the inner skin surface, the radiation penetration time is abbreviated as the outer surface temperature of the skin approaches the ambient temperature, with minimal correlation to the radiation Biot number. Conversely, convection flow, characterized by a higher Biot number, induces a brief surge in the inner skin temperature. Typically, the critical juncture for fuel tank temperature arises during the ascent phase immediately post-takeoff^[18], wherein the flight Mach number escalates substantially while the flight altitude experiences minimal change. Consequently, the boundary layer temperature and convection heat transfer coefficient witness significant increments, signifying a scenario marked by large radiation Biot numbers and Biot numbers. During this phase, heightened heat flow on the skin's exterior briefly penetrates the skin, elevating the inner skin temperature. Hence, the higher thermal conductivity of traditional metal fuel tanks effectively mitigates the impact of these two dimensionless parameters. However, advanced carbon fiber composite fuel tanks exhibit lower thermal conductivity than metal, escalating the two dimensionless parameter values. Consequently, the inner skin temperature increases. Therefore, it's imperative to accurately compute the temperature of composite fuel tanks with a Biot number exceeding 0.1.

6 Conclusion

The inner surface temperature of the skin can be efficiently and swiftly determined using an approximate solution when external thermal loads are imposed on the fuel tank of a civil aircraft. To validate the accuracy of this computational approach, comparisons are made with the analytical solution provided in standard heat transfer textbooks and numerical solutions obtained through finite difference numerical methods implemented

in MATLAB/Simulink. Upon verification, it's observed that the error tends to be more prominent only in scenarios with higher radiation Biot numbers. However, in other cases, the absolute error of the approximate solution remains within the acceptable range of 0.07. Such precision meets the requirements for unsteady heat transfer calculations of fuel tanks fabricated from various materials.

Analysis reveals that the aircraft's flight Mach number and flight altitude influence the convection coefficient and average boundary layer temperature, which are directly proportional to the dimensionless parameters Biot number and radiation Biot number. Consequently, increasing these dimensionless parameters results in a more significant temperature gradient within the skin. Moreover, it's inferred from the equations and diagrams that the maximum value of the inner surface temperature of advanced carbon fiber composite fuel tanks exceeds that of conventional metal fuel tanks when only considering aerodynamic fluid heat loads. Regarding airworthiness certification, addressing the flammability concerns associated with composite fuel tanks holds significant research value.

References:

- [1] Biot M A. New Methods in Heat Flow Analysis With Application to Flight Structures[J]. *Journal of the Aeronautical Sciences*, 1957, 24(12): 857-873.
- [2] Goodman T R. Application of Integral Methods to Transient Nonlinear Heat Transfer[M] Irvine T F, Hartnett J P. *Advances in Heat Transfer*. Elsevier, 1964: 51-122.
- [3] Goodman T R. The Heat-Balance Integral and Its Application to Problems Involving a Change of Phase[J]. *Journal of Fluids Engineering*, 1958, 80(2): 335-342.
- [4] Goodman T R. The Heating of Slabs with Arbitrary Heat Inputs[J]. *Journal of the Aerospace Sciences*, 1959, 26(3): 187-188.
- [5] Liao S, Su J, Chwang A T. Series solutions for a nonlinear model of combined convective and radiative cooling of a spherical body[J]. *International Journal of Heat and Mass Transfer*, 2006, 49(15-16): 2437-2445.
- [6] Tan Z, Su G, Su J. Improved lumped models for combined convective and radiative cooling of a wall[J]. *Applied Thermal Engineering*, 2009, 29(11-12): 2439-2443.
- [7] Crosbie A L, Viskanta R. Transient heating or cooling of a plate by combined convection and radiation[J]. *International Journal of Heat and Mass Transfer*, 1968, 11(2): 305-317.
- [8] Davies T W. Transient conduction in a plate with counteracting convection and thermal radiation at the boundaries[J]. *Applied Mathematical Modelling*, 1985, 9(5): 337-340.
- [9] Haseli Y, Naterer G F. Transient Heat Conduction in a Planar Slab With Convection and Radiation Effects[J]. *Journal of Heat Transfer*, 2022, 144(12): 121401.
- [10] Zierep J, Bühler K. *Hydro- and Aerostatics[M]*. Principles of Fluid Mechanics. Wiesbaden: Springer Fachmedien Wiesbaden, 2022: 35-50.
- [11] Sun H F. Numerical simulation of forehead aerodynamic heat transfer of high speed aircraft[M]. Harbin: Harbin Institute of Technology, 2008.
- [12] Gong Y. Air bus steady-state thermal load calculation of the cockpit[M]. NanJing: NanJing University of Aeronautics and Astronautics, 2010.
- [13] Aircraft Design Manual Total editorial board. Aircraft Design Manual volume 15: Life support and environmental control system design[M]. Beijing: Aviation Industry Press, 1999.

- [14] Yi CAO. Research on Calculation Method of External Convective Heat Transfer Coefficient of Civil Aircraft[C]//Proceedings of 2019 International Conference on Power, Energy, Environment and Material Science (PEEMS 2019). Advanced Science and Technology Application Research Center, 2019: 5.
- [15] Parmelee G V, Huebscher R G. Heat transfer by forced convection along a smooth flat surface[J]. Heat Piping Air Conditioning Engineer, 1947, 19(8): 115-122.
- [16] Haseli Y, Van Oijen J A, De Goey L P H. Analytical solutions for prediction of the ignition time of wood particles based on a time and space integral method[J]. Thermochemica Acta, 2012, 548: 65-75.
- [17] FAA. Fuel Tank Flammability Assessment Method(Monte Carlo Model) Version10[S]. Federal Aviation Administration, 2007.
- [18] Lv Y G, Ren G Z, Liu Z X, et al. Thermal analysis of fuel tank for aircraft[J]. Tuijin Jishu/Journal of Propulsion Technology, 2015, 36(1): 61-67.
- [19] Yang S M, Tao W Q, Heat Transfer Theory[M]. Beijing: High Education Press, 2006.